

Modeling of nonequilibrium surface growth by a limited mobility model with distributed diffusion length

Thomas Martynec* and Sabine H. L. Klapp†

Institut für Theoretische Physik, Technische Universität Berlin, Hardenbergstr. 36, 10623 Berlin, Germany

(Dated: March 21, 2019)

Kinetic Monte-Carlo (KMC) simulations are a well-established numerical tool to investigate the time-dependent surface morphology in molecular beam epitaxy (MBE) experiments. One drawback of the KMC method, however, is the high computational cost at growth conditions, where particle diffusion dominates over particle adsorption. As an alternative, we introduce in this study a limited mobility (LM) model to realistically simulate the low-temperature regime (where detachment processes can be neglected). The model is based on the stochastic transition rules of the so-called Das Sarma-Tamborena (DT) model, but differs from the latter via a variable diffusion length. A first guess for this length can be extracted from the mean-squared displacement calculated from short KMC simulations. Comparing the resulting surface morphologies in the submonolayer growth regime to those obtained from KMC simulations, we find deviations which can be cured by adding fluctuations to the diffusion length. This mimics the stochastic nature of particle diffusion on a substrate, an aspect which is usually neglected in LM models. We propose to add fluctuations to the diffusion length by choosing this quantity for each adsorbed particle from a Gaussian distribution. The analysis of the surface morphologies (on one-dimensional substrates) in the sub- and multilayer growth regime shows that the LM model is capable of producing structures that are indistinguishable to the ones from KMC simulations at arbitrary growth conditions. Our method can be generalized to two-dimensional calculations.

I. INTRODUCTION

Nonequilibrium surface growth by means of molecular beam epitaxy (MBE) is one of the most widely used techniques to fabricate thin film devices for various technological applications [1–4]. Since the growth conditions can be precisely controlled, MBE also serves as an exemplary experimental setup to study fundamental aspects of nonequilibrium statistical mechanics [5–7].

The time-dependent morphologies in MBE evolve due to a competition between adsorption of particles on the system’s surface, on the one hand, and diffusion processes, on the other hand. Particles like atoms, organic molecules or colloids get adsorbed on a flat and defect-free substrate (ideal growth conditions) at rate F , which is typically given in deposited monolayers (ML) per second (ML/s) [5–8]. The adsorption is followed by thermally activated (Arrhenius-type) diffusion processes with energy-dependent rates $D(T) = \nu_0 \exp(-E_A/k_B T)$, where $\nu_0 = 2k_B T/h$ is the attempt frequency (with k_B being the Boltzmann constant, h the Planck constant and T the substrate temperature) and E_A the activation energy that consists of different energetic contributions. “Free” particles, i.e., particles without in-plane bonds towards particles on neighboring sites, diffuse laterally on the substrate at rate $D^0(T)$ until they participate in a cluster formation event (nucleation), or attach to an existing cluster. Depending on the details of the system (i.e., the type of deposited particles and substrate material) and the growth conditions, that is, the tempera-

ture T and adsorption rate F , the surface evolves either smooth or rough. Commonly, the growth conditions are expressed by the growth parameter

$$R = R(T, F) = D^0(T)/F. \quad (1)$$

The experimental morphologies seen in MBE experiments can be mimicked by numerical simulations [9, 10]. A popular strategy is to employ lattice models that are based on activation energy-dependent hopping rates for all particles in the topmost layer. These models are often referred to as “full diffusion” or Arrhenius-type models [11–21]. One major example is the (event-driven) kinetic Monte-Carlo (KMC) method based on the Clarke-Vvedensky bond-counting Ansatz [22] involving diffusion to nearest-neighbor lattice sites. Given the correct, system-specific values of all relevant energy barriers that contribute to the activation energy E_A , KMC simulations have indeed proven to be a powerful simulation technique capable of describing the surface growth of a variety of real systems [9, 10, 23–25].

However, from a practical point of view, KMC simulations are typically limited to rather *low* surface temperatures T or *high* adsorption rates F (i.e., small values of R) and to relatively small systems sizes L (with L being the length of the simulation box). This restriction has to do with the large computational effort required to simulate the trajectories of the freely diffusing particles, without making much progress in the actual time evolution of the system.

The computational time can be strongly reduced by using a class of growth models that are known as limited mobility (LM) models [26–30]. Here, the process rates that are used in KMC simulations are replaced by a cer-

* martyne@tu-berlin.de

† klapp@physik.tu-berlin.de

tain set of stochastic rules for particle movements that depend on the local environment of the position of particle adsorption. Importantly, the deposited particles only perform one single movement that depends on the specific rules of the underlying LM model. Well-known examples of LM models with surface diffusion include the Family (F) model [26], the Wolf-Villain (WV) model [27, 28] and the model of Das Sarma and Tamborenea (DT) [29, 30].

In the present study, we introduce an extended version of the DT model since the latter is particularly suitable to describe *low* temperature MBE growth (detachment processes can be essentially neglected). In the original version of the DT model [29], adsorbed particles only explore the nearest neighbors of the adsorption site. This scenario corresponds to a diffusion length $l = 1$ (in units of the lattice constant). However, under realistic conditions for MBE growth, the average diffusion length of adsorbed particles is usually $l > 1$, a situation that has been hardly studied in the literature [34–38]. Studying the case $l > 1$ generally requires the use of various fit parameters in the chosen LM model to match the results of corresponding KMC simulations. Here, we employ a LM model with fit parameters that are based on physical quantities only. Extending the DT model towards $l > 1$ implies that we have to find a prescription of how to choose l for a given value of R [see Eq. (1)]. This is the main objective of the present paper.

More specifically, we aim to choose the value of l based on an appropriate quantity calculated by (short) KMC simulations. In other words, we seek a mapping procedure between the two type of models. The goal is that the resulting LM model produces surface structures identical to those obtained from KMC simulations (and therefore also identical to *low* temperature MBE growth) at any value of R with, at the same time, highly reduced computational effort. In this way, the LM model can be used to simulate MBE growth at growth conditions that are typically inaccessible to KMC simulations. This would enable us, for example, to study the asymptotic regime of the surface growth where we expect to observe scaling behavior of the growing surface. In particular, one would like to extract the corresponding critical exponents describing the scaling of the surface roughness [44] without being limited by finite-size effects or computational manipulations like the noise reduction technique (NRT) [39–43].

The remainder of the manuscript is structured as follows. In Sec. II, the KMC model and the LM model are introduced and explained in detail. In line with other studies in this area [34–38], we focus on the one-dimensional case. Following this, we establish in Sec. IIIB a relation between R and l to connect both models. A numerical analysis and comparison of the two models in the sub- and multilayer growth regime at various growth conditions is given in Sec. IIIC - IIID. There, we also highlight the importance of introducing fluctuations in the diffusion length when $l > 1$. Finally, we conclude in Sec. IV, where we also give a brief outlook towards

the experimental relevant two-dimensional case.

II. SIMULATIONS DETAILS

A. System settings

All simulations in this study were performed on one-dimensional substrates with discrete, equidistant positions $i = 1, 2, \dots, L$ (see Fig. 1 for an illustration). The corresponding local surface heights are given by the integers h_i (i.e., $h_i = 0$ corresponds to an empty site). These integers form the vector

$$\mathcal{H} = [h_1, h_2, h_3, \dots, h_{L-1}, h_L]. \quad (2)$$

We apply periodic boundary conditions and the solid-on-solid condition, that is, vacancies and overhanging particles are not allowed. As a consequence, the spatially averaged surface height on the lattice at time t is given by

$$\langle h(t) \rangle = \frac{1}{L} \sum_{i=1}^L h_i(t) = Ft, \quad (3)$$

where the expression on the right side corresponds to the number of deposited particles (expressed in monolayer, with $1 \text{ ML} \hat{=} L$ particles). The product Ft is henceforth referred to as coverage $\theta(t) = Ft$. Therefore, time-dependent quantities can also be expressed as functions of $\theta(t)$. Throughout this work, we characterize the growth conditions via the dimensionless, free diffusion to adsorption ratio $R(T, F)$ defined in Eq. (1).

B. The kinetic Monte-Carlo model

Within the KMC method, particles are adsorbed on randomly chosen lattice sites i with an (effective) adsorption rate F . The adsorption process is followed by diffusion processes from site i to nearest-neighbor lattice sites $j = i \pm 1$. Following the Clarke-Vvedensky bond-counting Ansatz [22], the hopping rates are given by

$$D_{ij} = \nu_0 \exp(-E_A/kT), \quad (4)$$

with activation energy

$$E_A = E_D + nE_N. \quad (5)$$

In Eq. (5), E_D is the energy barrier for free diffusion, which we set to $E_D = 0.5 \text{ eV}$ in all KMC simulations in this study. We use this value for E_D because it is close to the known diffusion barriers of various, intensely studied, atomic and organic systems [9, 10], and because

this choice is consistent with previous KMC studies [9, 15]. The rate for free diffusion to neighboring lattice sites is then given by

$$D_{ij}^0 = \nu_0 \exp(-E_D/kT) \equiv D^0(T). \quad (6)$$

The additional energy contribution E_N in Eq. (5) stems from interactions with nearest-neighbors in lateral directions. Here, n is the number of such bonds. In one dimension, this number can take the values $n = 0, 1, 2$. We here choose a high value of E_N , that is, $E_N = 1.0$ eV, in order to mimic MBE growth at *low* T . Then, already one in-plane bond is sufficient to suppress further diffusion. In other words, particles immediately immobilize once they sit on a lattice site i with $n > 0$. Consequently, already dimers represent stable clusters, and the critical island size i^* is one [55].

A typical KMC simulation consists of a large number of iterations p . In each iteration step, a particle either performs a hopping process from site i to a neighboring lattice site $j = i \pm 1$, or a new particle gets adsorbed. The simulation time (with $t_0 = 0$ being the starting time) after p iteration steps is updated stochastically as

$$t_{p+1} = t_p + \tau, \quad (7)$$

where τ is defined as

$$\tau = -\frac{\ln(X)}{r_{\text{all}}}. \quad (8)$$

Here, $X \in (0, 1)$ is a random number chosen uniformly from the given interval, and

$$r_{\text{all}} = \sum_{i=1}^L \left(\sum_{j=1}^2 D_{ij} + F \right) \quad (9)$$

is the sum of rates related to all particles in the top-most layer of the discretized (one dimensional) lattice.

For simplicity, we do not consider an additional energy barrier E_{ES} for inter-layer diffusion processes across step-edges, usually referred to as Ehrlich-Schwoebel barrier [52–54]. However, such a barrier could be included, in principle. The temperature is fixed to $T = 273$ K in all KMC simulations in this study. In order to realize different growth conditions expressed via the growth parameter $R = D^0(T)/F$, we use F as a variable.

C. The limited mobility model

The second model we investigate falls into the class of limited mobility models. Specifically, we consider a variant of the intensively studied model by Das Sarma and Tamborenea (DT model), in which the diffusion length

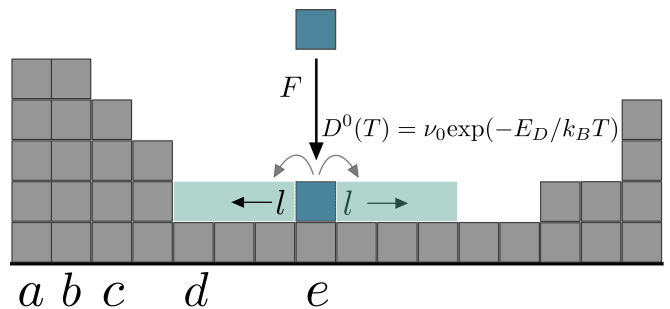


FIG. 1. Illustration of particle deposition and surface relaxation in the system that is used to simulate low temperature MBE surface growth. The quantities F and $D^0(T)$ refer to the KMC simulation, while the diffusion length l is characteristic for the LM model.

is restricted to one lattice constant ($l = 1$) [29, 30]. In contrast, here we consider the case $l \geq 1$ [34, 37, 38].

To clarify our approach, we first summarize the algorithm of the original DT model. In each iteration step, a particle is adsorbed at a randomly chosen lattice site $i \in [1, L]$. If the particle has at least one in-plane nearest-neighbor on this position i , it will stick there permanently. Otherwise, the particle is allowed to hop either to the left neighboring site, $j = i - 1$, or to the right neighboring site, $j = i + 1$, if one of these two sites provides at least one in-plane bond. If both sites provide at least one such lateral bond, one of the two sites is chosen randomly and the particle hops to site j and sticks there for the rest of the simulation. If none of the neighboring sites provides lateral bonds, the particle will remain at the initial adsorption site i .

Note that when a particle gets adsorbed at site i , the corresponding surface height increases by one, i.e., $h_i \rightarrow h_i + 1$. In-plane bonds for a particle adsorbed at site i are present if $h_i + 1 \leq h_j$ ($j = i \pm 1$). If the site provides exactly one in-plane bond ($n = 1$), it is called kink site, while a site that provides two such bonds ($n = 2$) is called a valley site. Since particles with $n \geq 1$ are immobile, the DT model represents a minimal model for MBE growth at *low* T . In this situation, already one in-plane bond is enough to suppress particle diffusion.

As an illustration of the DT model, consider a particle adsorbed at site b in Fig. 1. This site is characterized by $n = 0$, therefore, the particle will diffuse. Since site a (left neighbor) does not provide a bond, the particle will diffuse to site c , which provides one in-plane bond ($n = 1$). Indeed, the particle will stick there permanently for the rest of the simulation. For the same reason, a particle adsorbed at site c will stick there without diffusing to a neighboring lattice site because it already has one bond at this site. The same holds for a particle adsorbed at site d . A different situation arises for a particle adsorbed at site e . This site is characterized by $n = 0$, however, the particle is going to remain there because the two neighboring sites do not provide in-plane bonds ($n = 0$ at sites $j = e \pm 1$). Immediately after the particle has

found its final position, the next particle gets adsorbed. Due to this dynamics, the system is also said to exhibit instantaneous relaxation.

In the present study, we extend the DT model by allowing adsorbed particles to explore not only nearest-neighbor lattices sites ($j = i \pm l$, with $l = 1$) to diffuse to kink or valley sites, but also to sites that are farther away from the initial adsorption site i . In other words, we consider the case $l \geq 1$ ($j = i \pm l$, with $l > 1$). In the following we refer this variant of the DT model to as LM model. This is exemplarily illustrated in Fig. 1 by the blue shaded region that corresponds to diffusion length $l = 3$. In the original version of the DT model, a particle adsorbed at site e would remain there, while for $l = 3$ it is relocated to site d since this site provides one in-plane bond ($n = 1$).

III. CONNECTING BOTH MODELS

A. Strategy

It is well established that the surface morphologies observed in MBE (and KMC) depend on the growth parameter $R(T, F)$ [see Eq. (1)]. The latter determines, in particular, the cluster properties in the submonolayer as well as the overall morphology of the surface in the multilayer growth regime. Our aim is to establish a direct connection between the KMC and the LM model with $l > 1$ in order to mimic growth by the KMC model at any value of $R(T, F)$ (in the following we only use R).

To compare the resulting morphologies in the submonolayer regime ($\theta < 1$), we calculate the total number of clusters on the lattice, $N(\theta)$, as function of the coverage θ and the island size distribution, $P(S)$, at various values of the growth parameters R . In the multilayer regime, we calculate layer coverages θ_k (with k being the layer index) and compute the global interface width $W(L, \theta)$ in order to compare the models. In the regime of saturated surface roughness, we additionally investigate fluctuations of $W(L, \theta)$ around the mean saturation value, $W_{sat}(L)$. If all these measured quantities match in both models for all values of the growth parameter R , we conclude that the LM model with variable l correctly mimics the structures produced in KMC simulations.

Therefore, our main objective of this study is to find a consistent relation between the growth parameter R in the KMC model, on the one hand, and the diffusion length l in the LM model, on the other hand, such that the resulting surface morphologies are indistinguishable.

B. Diffusion properties

1. Mean-squared displacement and nucleation length

As a starting point, we first calculate via KMC simulations the mean-squared displacement (MSD) of adsorbed

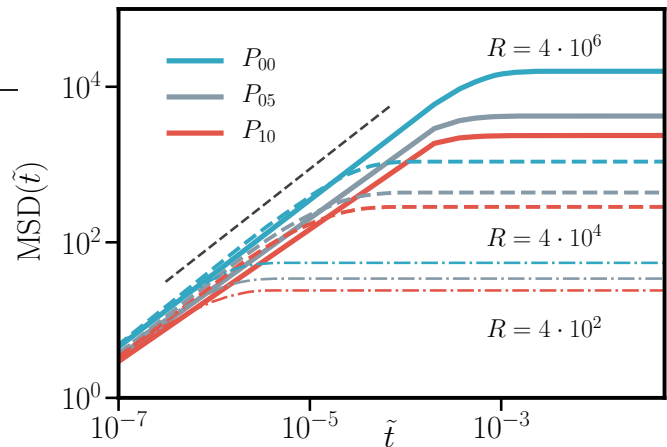


FIG. 2. KMC results for the mean-squared displacement (MSD) as function of time \tilde{t} for individual particles adsorbed at coverage $\theta = 0.0$ (P_{00}), $\theta = 0.05$ (P_{05}) and $\theta = 0.10$ (P_{10}) for three different values of the growth parameters R .

particles as function of time \tilde{t} that individual particles spend on the lattice. The MSD is defined as

$$MSD(\tilde{t}) = \langle (i(\tilde{t}) - i(0))^2 \rangle. \quad (10)$$

Here, $i(\tilde{t}) \in [1, L]$ represents the discrete position of the particle on the lattice at time \tilde{t} , and $i(0)$ is the initial adsorption site where the particle has adsorbed at $\tilde{t} = 0$. Further, $\langle \dots \rangle$ is an average over many realizations. Depending on the growth conditions, $MSD(\tilde{t})$ saturates at a characteristic time \tilde{t}_S and corresponding value $MSD_S = MSD(\tilde{t}_S)$. This reflects the immobilization induced by the formation of in-plane bonds towards particles on neighboring lattice sites. In each simulation run, only one particle is tracked and we average over $\mathcal{O}(10^5)$ realizations. We separately consider particles of type P_θ that are adsorbed at specific coverages θ during submonolayer growth. The specific particle types that we track are P_{00} , which corresponds to the first adsorbed particle ($\theta = 0.00$), P_{05} (particle adsorbed at $\theta = 0.05$) and P_{10} (particle adsorbed at $\theta = 0.10$). All particles are monitored up to a final coverage of $\theta = 0.5$ to ensure that MSD_S is reached.

Results for $MSD(\tilde{t})$ at three representative values of R are shown in Fig. 2. At short times \tilde{t} we observe normal diffusive behavior, that is, $MSD(\tilde{t}) \propto \tilde{t}$ for all R and P_θ . This regime is followed by a flattening of $MSD(\tilde{t})$ until, depending on R and P_θ , saturation sets in at \tilde{t}_S and MSD_S . Upon decrease of R from high values, \tilde{t}_S decreases and so does MSD_S . This can be explained as follows. The smaller R , the more the surface growth is dominated by adsorption of particles rather than by diffusion. Consequently, the average time interval $\Delta t = 1/F \sim R$ between two subsequent adsorption events becomes smaller. Thus, at small values of R , particles have a higher chance to form in-plane bonds than

at larger R . On average, they therefore diffuse over a shorter time \tilde{t}_S and length $\sqrt{MSD_S}$ compared to particles in simulations at larger R .

Moreover, we notice that the value of MSD_S at fixed R depends on the type of particle, P_θ . In particular, we see that MSD_S for P_{00} is higher than for P_{05} and P_{10} at any value of R . Henceforth, we therefore focus on particles of type P_{00} , since they diffuse the maximum possible distance (i.e., the distance before reaching saturation due to immobilization) at given R . To quantify this distance for particles P_{00} , we define the "nucleation length"

$$l_n(R) = \sqrt{MSD_S|_{P_{00}}(R)}. \quad (11)$$

Clearly, this quantity depends on R (see Fig. 2).

2. Geometrical cluster distance

An additional (and experimentally accessible) measure for the distance which a particle travels until getting immobilized, is the "geometrical cluster distance". This quantity (for a d -dimensional system) is given by

$$d_g(R) = \left(\frac{L^d}{N_{max}(R)} \right)^{1/d}, \quad (12)$$

where $N_{max}(R)$ is the maximum number of clusters in the first layer in the submonolayer growth regime (at given R), and L is the linear system size.

3. Scaling of l_n and d_g as function of R

As stated before, our goal in this section is to find a relation between the "diffusion length" l determining the LM model, and the growth parameter R . Given the results in the previous subsection, the question arises whether l_n [see Eq. (11)] or d_g [see Eq. (12)] might serve as an appropriate choice for l . To explore this issue, we plot l_n along with d_g as function of R (in the experimentally relevant regime) in Fig. 3. For values $R < 10^3$, particle adsorption dominates, and we observe that l_n increases with R , while d_g remains nearly constant. As we enter the regime $R \geq 10^3$, particle diffusion begins to dominate and we identify the scaling relation

$$l_n \approx d_g \sim R^{1/3}. \quad (13)$$

The result that d_g scales with R with exponent $\gamma = 1/3$ is indeed not too surprising. To this end, we recall that $d_g \sim 1/N_{max}$ [see Eq. (12)]. It is well established [55] that the maximum number of clusters, N_{max} , fulfills the scaling relation

$$N_{max} \sim R^{-\chi}, \quad (14)$$

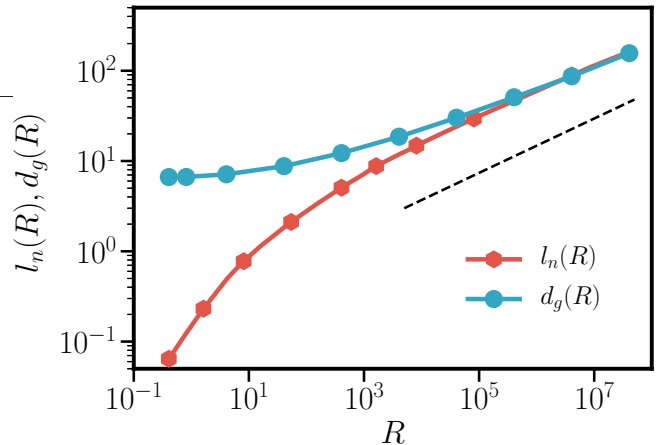


FIG. 3. KMC results for the nucleation length l_n [see Eq. (11)] of particles adsorbed at the very early stage of submonolayer growth, and the geometrical distance d_g [see Eq. (12)] between clusters, as function of R . The dotted black line describes the dependency $\sim R^\gamma$, with $\gamma = 1/3$.

where $\chi = i^*/(i^* + 2)$ (with i^* being the critical cluster size). In the present case we have $i^* = 1$ (irreversible cluster growth) and, thus, $\chi = 1/3$. It then follows immediately that $d_g \sim R^{1/3}$.

The more intriguing result is that l_n follows the *same* scaling and takes (approximately) the same values. This means that it is sufficient to know N_{max} (which can be experimentally determined from AFM or STM snapshots) to find both lengths, l_n and d_g .

Based on these findings, we henceforth take the nucleation length l_n (or, equivalently, d_g for $R \geq 10^3$) as an estimate for the diffusion length l in the LM model. In the following, we analyze corresponding numerical results in detail.

C. The submonolayer growth regime

In this section, we aim at investigating whether the LM model with $l = l_n(R)$ can indeed reproduce morphologies in the submonolayer regime ($\theta < 1$) that are equivalent to those obtained in KMC simulations at arbitrary values of R . To compare the two models quantitatively, we calculate $N(\theta)$, the number of clusters in the first layer, as well as the corresponding distribution $P(S)$ of clusters of size S .

1. Results for fixed diffusion length l

The evolution of $N(\theta)$ for various values of the growth parameter R is shown in Fig. 4. We here focus on the regime $\theta < 1$ corresponding to submonolayer growth. In this regime, we observe good agreement between the KMC and the LM model at the lowest value of R con-

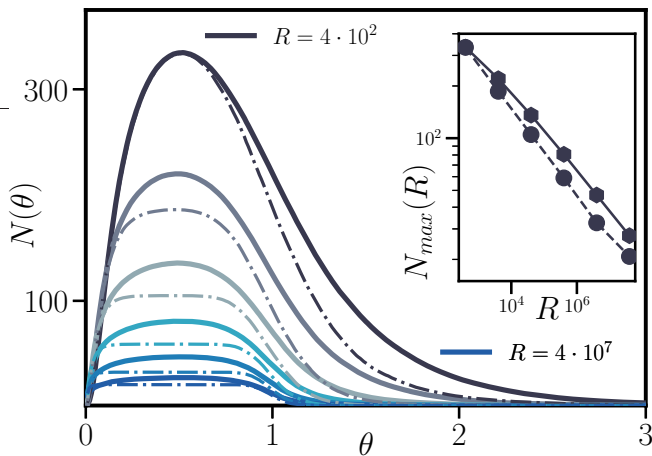


FIG. 4. Comparison of $N(\theta)$ up to $\theta = 3.0$ in the KMC model for various values of R (solid lines) and the LM model (dotted lines) with fixed diffusion length $l = l_n(R)$ (see Fig. 3) for all deposited particles. The inset shows the maximum number of clusters, N_{max} , as function of R in both models.

sidered, $R = 4 \cdot 10^2$ (corresponding to $l = 5$). In particular, the location and height of the maximum, N_{max} , is matching perfectly. However, for larger values of R , we find pronounced deviations. Particularly striking are the discrepancies in N_{max} and the emergence of a plateau in $N(\theta)$ within the LM model in comparison to KMC simulations with $R \geq 10^3$. This shows that at growth conditions where diffusion dominates over adsorption, the LM model fails to correctly reproduce the KMC simulations.

Considering $P(S)$ at three different coverages ($\theta = 0.25$, $\theta = 0.5$ and $\theta = 0.75$) and different values of R , we observe a similar behavior (see Fig. 5). While $P(S)$ in both models is nearly identical (at all θ considered) at $R = 4 \cdot 10^2$ ($l = 5$), this agreement vanishes at larger values of R and corresponding values for l . In particular, we observe a narrowing of $P(S)$ and a shift of the main peak towards larger cluster sizes according to the LM model in comparison to $P(S)$ obtained from KMC simulations. Combined with our previous findings for $N(\theta)$, we conclude that the LM model yields fewer, more regular clusters which are, however, on average larger than those obtained in KMC simulations.

The discrepancy between KMC and LM results for $R > 4 \cdot 10^2$ is further confirmed by the exemplary lattice structures shown in Fig. 6. The structures are obtained at $\theta = 0.25$ from simulations with $L = 16384$. While for $R = 4 \cdot 10^2$ ($l = 5$), the cluster ensemble in both models looks quite similar, we observe remarkable differences at $R = 4 \cdot 10^5$ ($l = 46$). As already indicated by $N(\theta)$ and $P(S)$, one can directly see that the number of clusters is lower, and, additionally, the cluster sizes are too regular in the LM model compared to the corresponding ensemble of clusters obtained from KMC simulations.

Our reasoning for the observed discrepancies at values $R > 4 \cdot 10^2$ is the following. Nonequilibrium surface

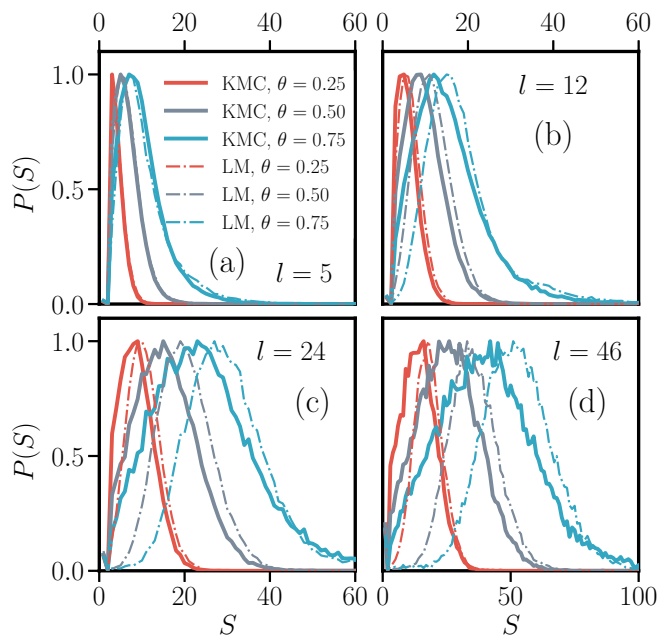


FIG. 5. Comparison of the island size distribution $P(S)$ at three different stages of submonolayer growth ($\theta = 0.25$, $\theta = 0.5$ and $\theta = 0.75$) and four different values of R , leading to four values of l . Solid lines correspond to data from the KMC model, while dashed-dotted lines to the LM model with fixed diffusion length $l = l_n(R)$ for all particles.

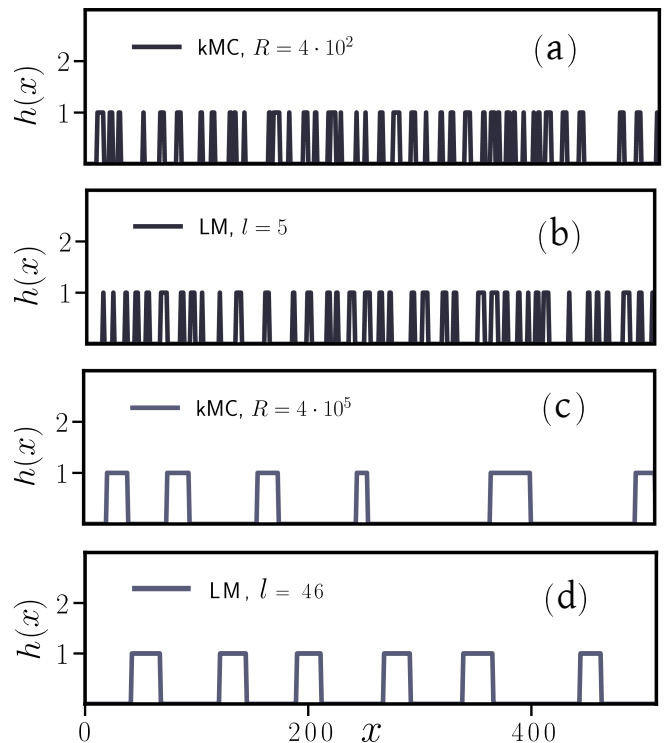


FIG. 6. Comparison of cluster structures obtained from the KMC model at $\theta = 0.25$ [(a) and (c)] and the LM model [(b) and (d)] for two different values of the growth parameters R and the corresponding diffusion length $l = l_n(R)$.

growth is dominated by stochastic processes that involve fluctuations not only in the deposition, but also in the diffusive motion of the particles. By setting a *constant* diffusion length l in the LM model, this fundamental aspect is fully neglected. As a consequence, we obtain less clusters which are, moreover, too regular and equidistant as opposed to the clusters in the KMC simulations, where the stochastic nature of diffusion is included. While the fluctuations in diffusion seem to be irrelevant at $R \leq 4 \cdot 10^2$, they do become significant for growth conditions where diffusion dominates ($R > 10^3$). This suggests that, in order to realistically model nonequilibrium surface growth in the LM model at larger values of R , one has to introduce diffusional fluctuations "by hand".

2. Adding fluctuations to the diffusion length l

Our strategy to add fluctuations to the diffusion processes in the LM model is as follows. Instead of taking a fixed diffusion length $l = l_n(R)$ for all particles, we choose l individually for each particle from a Gaussian distribution given by

$$P(l | l_n, \sigma^2) = \frac{1}{\sqrt{2\pi\sigma^2}} \exp\left[-\frac{l - l_n(R)}{2\sigma^2}\right]. \quad (15)$$

The distribution has its maximum at the diffusion length $l = l_n(R)$ resulting from the corresponding KMC simulations (see Fig. 3), while the variance σ^2 serves as an adjustable parameter that controls the strength of fluctuations. The larger the value of R , the more time the particles in KMC simulations spend by freely diffusing on the lattice. Consequently (since free diffusion is a Gaussian process), the broader is the normal distribution of the distances traveled within this time. In the LM model, we mimic this effect by increasing σ^2 with R . Note that in the limit $\sigma^2 \rightarrow 0$, $P(l | l_n, \sigma^2)$ transforms into a delta function. This corresponds to the original version of our LM model where l is the same for all adsorbed particles.

To test the ansatz given in Eq. (15), we show in Fig. 7 (a) - (c) KMC data for $N(\theta)$ at three values of R together with results from the LM model with different values of σ^2 . For all non-zero values of σ^2 (i.e., non-zero fluctuations), we observe an increase of N_{max} towards higher values compared to the case $\sigma^2 = 0$ where l is the same for all particles. Additionally, the unphysical plateau in $N(\theta)$, that is present in simulation results from the LM model (with $\sigma^2 = 0$) for coverages from $\theta \approx 0.2$ to $\theta \approx 0.8$ (see Fig. 4), vanishes. We note that if the fluctuations in l are too strong (i.e., σ^2 is chosen too large), we "overshoot" the values N_{max} from the corresponding KMC simulations. Indeed, by probing different values of the variance σ^2 we find, for all considered values of R , an *optimal* value of σ^2 [see Fig. 7 (d)] such that the LM model results for $N(\theta)$ are in good agreement with the KMC data. We take these optimal values of σ^2 [see Fig.

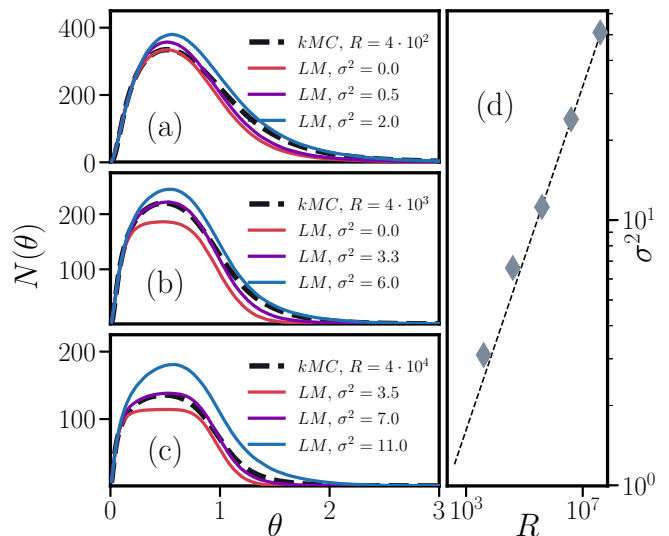


FIG. 7. (a-c) Comparison of $N(\theta)$ in the KMC and the LM model up to $\theta = 3$. The dotted line represents KMC results, while the solid lines are results of the LM model with fluctuations in l with optimal values for σ^2 that are chosen such that the LM model best fits the KMC data. (d) *Optimal* values for the variance σ^2 in l of the LM model that yield best fits of the functions $N(\theta)$ from KMC simulations. The straight dotted black line describes the dependency $\sim R^{1/3}$.

7 (d)] that best fit the KMC results for all further investigations.

In order to quantify the importance of adding fluctuations to l in the LM model, we present in Table I results for the relative error of the quantity N_{max} , $\epsilon(N_{max}) = |N_{max}^{LM} - N_{max}^{KMC}| / N_{max}^{KMC} \cdot 100$. Specifically, we compare results from the LM model with fixed l ($\sigma^2 = 0$) and variable l ($\sigma^2 > 0$) with corresponding values of N_{max} in the KMC model. Considering the data given in Table I, we find that for values $l \leq 5$ ($R \leq 4 \cdot 10^2$), the relative error in N_{max} is negligible for fixed, as well as for variable l with optimal σ^2 . However, as $l \geq 12$ ($R \geq 4 \cdot 10^3$), $\epsilon(N_{max})$ in the LM model with $\sigma^2 = 0$ becomes significant and increases as function of l , reaching $\epsilon(N_{max}) = 30.64\%$ for $l = 88$ ($R = 4 \cdot 10^6$). In contrast, the error in presence of fluctuations in l remains below $\epsilon(N_{max}) = 2\%$ for all considered growth conditions.

In fact, as shown in Fig. 8, our approach also helps to overcome the discrepancies in $P(S)$ observed in Fig. 5 (where $\sigma^2 = 0$). Given the appropriate value for σ^2 in $P(l | l_n, \sigma^2)$, the peaks of $P(S)$ in the data from the LM model are shifted towards those obtained from KMC simulations. Furthermore, with the optimal values for σ^2 , $P(S)$ is broader compared to the situation where fluctuations in l are absent, reflecting a more diverse composition of clusters as it is indeed the case in the KMC simulations [see Fig. 6 (c)].

TABLE I. Relative error ϵ (in %) of the maximum number of clusters N_{max} in the system during submonolayer growth.

l	$\sigma^2 = 0$	optimal σ^2
2	0.0771	0.0017
3	0.0816	0.0072
5	0.1052	0.0126
12	15.4116	0.7403
24	22.7099	1.7865
46	26.8857	1.2526
88	30.6446	0.2738

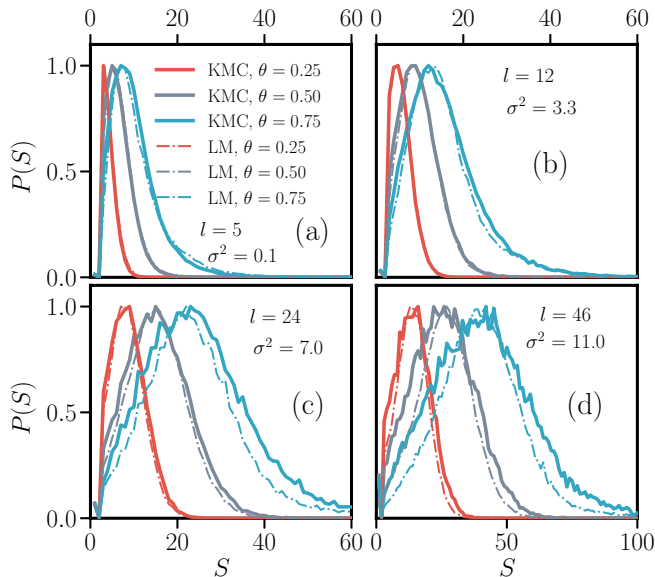


FIG. 8. Comparison of the island size distribution $P(S)$ at three different stages of submonolayer growth ($\theta = 0.25$, $\theta = 0.5$ and $\theta = 0.75$) for different values of R in the KMC and the LM model with fluctuations in the diffusion length l with optimal σ^2 [see Fig. 7 (d)].

D. The multilayer growth regime

Having found a suitable LM model to describe the submonolayer growth, it is an important question whether this model is also capable of describing multilayer growth. The main quantity of interest concerning the surface morphology in the multilayer regime is the global interface width [5, 26, 45, 46], defined as the root of the integrated mean square fluctuations of the local surface height at coverage θ . In continuous form, the global interface width in one dimension reads

$$W(L, \theta) = \sqrt{\frac{1}{L} \int_0^L (h(x, \theta) - \langle h(\theta) \rangle)^2 dx}. \quad (16)$$

Here, $h(x, \theta)$ is the local surface height at position x (or i in discrete form) and coverage θ , L is the size of the

substrate, and

$$\langle h(\theta) \rangle = \frac{1}{L} \int_0^L h(x, \theta) dx \quad (17)$$

represents the average surface height of the growing film. Thus, $W(L, \theta)$ is a measure of the surface roughness. Further, studying $W(L, \theta)$ allows to explore whether the dynamics of the growing surface exhibits universal behavior and can thus be assigned to one of the established universality classes in nonequilibrium surface growth [5, 8, 29–31, 47–51]. To be more specific, investigating $W(L, \theta)$ helps to identify whether the local surface height evolves (in the hydrodynamic limit) in the functional form $\partial_\theta h(x, \theta) = \mathcal{F}[\nabla^n h(x, \theta)]$, where \mathcal{F} is a characteristic functional involving gradient terms. Thus, examining $W(L, \theta)$ can contribute to a deeper understanding of the interface dynamics during MBE growth and may lead to improved control strategies for epitaxially fabricated devices.

Generally, the global interface width is known to follow the Family-Vicsek scaling relation [44]

$$W(L, \theta) \sim \theta^\beta f\left(\frac{L}{\theta^{1/z}}\right), \quad (18)$$

where β and z are the growth and dynamic exponent, respectively. Further, $f(u)$ is a scaling function that obeys

$$f(u) \sim \begin{cases} u^\alpha & u \ll 1 \\ \text{const.} & u \gg 1, \end{cases} \quad (19)$$

which involves the global roughness exponent $\alpha = \beta z$ that depends on the two independent exponents β and z . The set of these three critical exponents (α, β, z) determines the universality class of the growth process under study.

The growth exponent β can be extracted from the short-time behavior of the interface width which is known [44] to scale as $W(L, \theta) \sim \theta^\beta$ for coverages $\theta < \theta^*$ [with θ^* being the crossover coverage at which $W(L, \theta)$ reaches a saturation value $W_{sat}(L)$]. To obtain the exponents α and z , it is necessary to reach the asymptotic regime, $\theta \geq \theta^*$. Since the crossover coverage θ^* scales with system size L according to [44]

$$\theta^* \sim L^z, \quad (20)$$

it is very difficult to determine α and z for large L . This is due to the high computational demand to reach $W_{sat}(L)$, especially when $\alpha > 1$ and $z > 2$ [41–43].

1. From submonolayer to multilayer growth

We now explore whether the good agreement between the KMC and the LM model (with optimal σ^2), which was found in the submonolayer regime ($\theta < 1$) by analyzing $N(\theta)$ and $P(S)$, still holds when the surface growth proceeds towards multilayer structures, $\theta > 1$. In order to analyze the initial stages of multilayer growth, we compute the evolution of the coverage in the first ten layers in both models. In the following, layer coverages are denoted by θ_k , with k being the layer index. They are defined as

$$\theta_k = \frac{1}{L} \sum_{i=1}^L \Theta(|h_i - k|), \quad (21)$$

with the Heaviside step function $\Theta(X)$ that obeys $\Theta(X) = 0$ for $X < 0$ and $\Theta(X) = 1$ for $X \geq 0$. We note that θ_k is different from the quantity θ , since the latter describes the *total* coverage. The evolution of θ_k with θ gives a hint whether the surface after the formation of many layers will rather be smooth or rough. If the first layers are filled subsequently (layer-by-layer), the resulting surface will be smoother in comparison to a scenario where several layers are filled simultaneously.

Examples for these two scenarios are shown in Fig. 9 (a) and Fig. 9 (b), where θ_k (for $k = 1$ to $k = 10$) is plotted for two different values of R and corresponding distributions $P(l | l_n, \sigma^2)$. In Fig. 9 (a), where $R = 4 \cdot 10^2$, we observe that always more than one layer is filled at once. Different from that, we observe layer-by-layer filling in Fig. 9 (b) where $R = 4 \cdot 10^4$. In both cases, we find perfect agreement between the layer coverage evolution in both models considered. To show that this agreement holds at any value of the growth parameter R , we present in Fig. 9 (c) the evolution of $\theta_{10}(\theta)$ for various values of R and corresponding $P(l | l_n, \sigma^2)$. Again, we find nearly perfect agreement between results from both models. Thus, we can conclude that the LM model (with fluctuating diffusion length and optimally chosen variance) yields a very good description not only during submonolayer growth, but also during the early stages of multilayer growth.

2. The multilayer growth regime

In this section we study the regime of many layers (up to $\theta = 10^6$) by investigating the global interface width $W(L, \theta)$ [see Eq. (8)]. The evolution of $W(L, \theta)$ as function of θ for different system sizes L and four exemplary values of R and corresponding distributions $P(l | l_n, \sigma^2)$ is shown in Fig. 10. Results from KMC simulations are given by symbols, while for the LM model, $W(L, \theta)$ is represented by solid lines.

According to the Family-Vicsek scaling relation [44], the global interface width initially shows power-law scaling, $W(L, \theta) \sim \theta^\beta$. From our KMC data, we identify

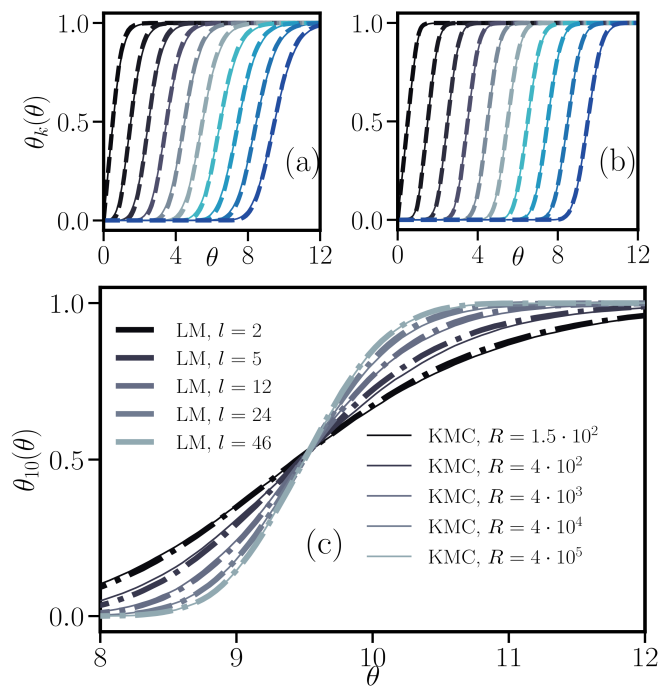


FIG. 9. (a) Evolution of the coverage in the first ten layers in the KMC model at $R = 10^2$ and $l = 5$ ($\sigma^2 = 0.1$) in the LM model. (b) The same at $R = 4 \cdot 10^4$ in the KMC model and $l = 24$ ($\sigma^2 = 7.0$) in the LM model. (c) Coverage evolution of the tenth layer at various growth conditions in both models. Solid lines represent KMC simulations, dotted lines are results from the LM model (with optimal variance σ^2).

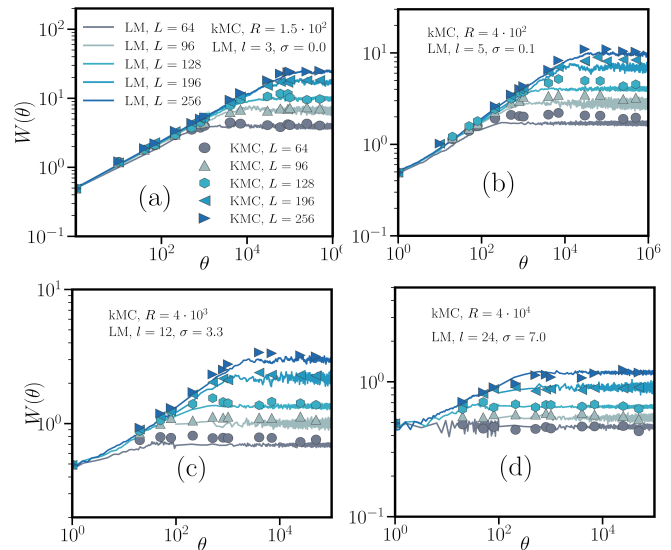


FIG. 10. Global interface width $W(L, \theta)$ as function of coverage θ for four different values of R in the KMC model (symbols) and corresponding diffusion length l in the LM model (solid lines) with optimal values for σ^2 for system sizes from $L = 64$ to $L = 256$.

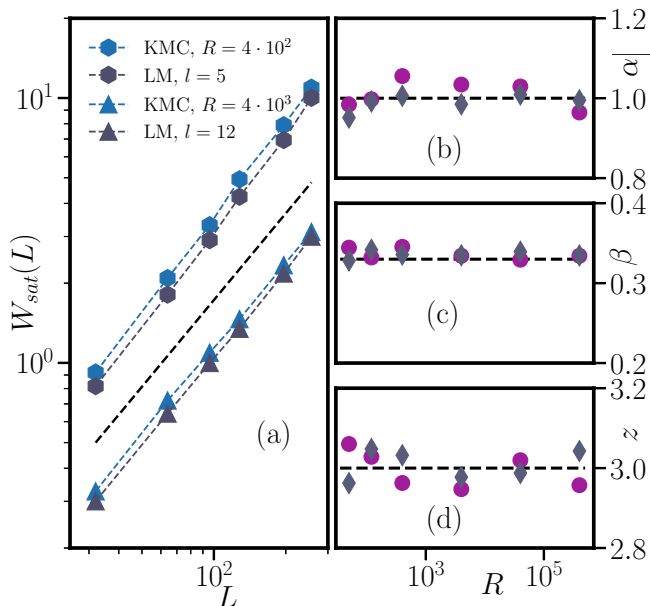


FIG. 11. (a) Scaling of the saturation roughness W_{sat} as function of system size L for two values of R in the KMC model and the corresponding values of l and σ^2 in the LM model (dotted black line $\sim L^1$). (b) Roughness exponent α , (c) growth exponent β and (d) dynamic exponent z for various growth conditions in both models. The lines in (b)-(d) represent the values of α, β, z according to the VLDS universality class in one dimension.

$\beta \approx 1/3$ for all considered values of R . The reason why β does not depend on R is that changing R does not change the symmetry properties of the system [51, 63, 64]. The growth exponent $\beta \approx 1/3$ also correctly describes the roughening in the transient regime in the LM model. Not only the scaling exponent $\beta \approx 1/3$ is the same in both models, but also the actual values of $W(L, \theta)$ for all considered values of R , corresponding distributions $P(l | l_n, \sigma^2)$ and system sizes L [see Fig. 11 (c)].

The transient regime is followed by a crossover to the asymptotic regime at the cross-over coverage θ^* , where the interface width reaches $W_{sat}(L)$. We find that, independent of the value of R and the corresponding distribution $P(l | l_n, \sigma^2)$, the onset of saturation of $W(L, \theta)$ at θ^* scales according to $\theta^* \sim L^3$ [see Eq. (20)]. Again, the scaling exponents are very similar in both models for all considered growth conditions [See Fig. 11 (d)].

In addition, we find that the saturation values obey $W_{sat}(L) \sim L^1$, as shown in Fig. 11 (b). Thus, the roughness exponent $\alpha \approx 1$ is the same for all considered growth conditions (and for both models).

At this point it is worth to recall that our LM model involves a fluctuating diffusion length, where the variance of the fluctuation (σ^2) is chosen based on data for sub-monolayer growth. To demonstrate the accuracy in the multilayer regime, we show in Fig. 12 the relative error $\epsilon(W_{sat}) = |W_{sat}(L)^{LM} - W_{sat}(L)^{KMC}| / W_{sat}(L)^{KMC} \cdot 100$ of $W_{sat}(L)$ for the LM model with $\sigma^2 = 0$ and the

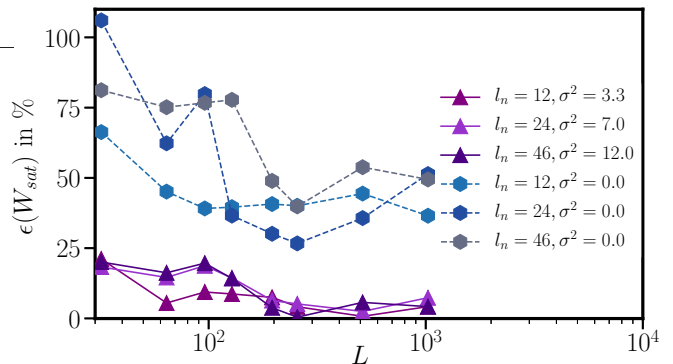


FIG. 12. Relative error $\epsilon(W_{sat})$ of the saturation roughness $W_{sat}(L)$ in the LM model compared to KMC simulations. Results for $\epsilon(W_{sat})$ without fluctuations in the diffusion length l (i.e., $\sigma^2 = 0$) are given by hexagons, while $\epsilon(W_{sat})$ with optimal σ^2 are represented by triangles.

version with optimal σ^2 . For all considered growth conditions we find that, as L is increased, $\epsilon(W_{sat})$ diminishes when the optimal σ^2 is used, while the error is $\geq 40\%$ in the absence of fluctuations in l ($\sigma^2 = 0$).

We now turn back to the scaling behavior. In summary, we identify the following critical exponents in our simulations: $\alpha \approx 1$, $\beta \approx 1/3$, $z \approx 3$ (for all growth conditions considered). As known from simulations and analytical calculations of the DT model (with $l = 1$), this set of critical exponents belongs to the Villain-Lai-Das Sarma (VLDS) universality class in one dimension [30, 31, 56]. The corresponding evolution equation for the surface height in the hydrodynamic limit is given by

$$\partial_t h(x, t) = -\nu_4 \partial_x^4 h(x, t) + \lambda_4 (\partial_x^2 h(x, t))^2 + F. \quad (22)$$

In Eq. (22), $h(x, t)$ is the surface height at position x at time t , ν_4 and λ_4 are constants, and F is a Gaussian white noise, representing the randomness accompanying the deposition of particles. Thus, Eq. (22) is a stochastic, nonlinear partial differential equation. Note that for $\lambda_4 = 0$ the equation reduces to the linear Mullins-Herring (MH) equation (characterized by the critical exponents, in one dimension, $\alpha = 3/2$, $\beta = 3/8$, $z = 4$) [32, 33]. The non-linear equation, $\lambda_4 \neq 0$, is known to have the same symmetry as several discrete lattice models (including the DT model) [29, 30] that are frequently used to model surface growth. Thus, the nonlinear equation displays the same set of critical exponents.

As known from experiments [57–59] and KMC simulations [60–62], the surface of a growing thin film becomes smoother as the value of R is increased. We systematically study this smoothing of the surface and the thus resulting decrease of the surface roughness in the extended LM model detail by plotting W_{sat} versus l for fixed system sizes L in Fig. 13 (a). For system sizes from $L = 64$ to $L = 256$ we find that $W_{sat}(L, l)$ obeys a power-law, $W_{sat}(L, l) \sim l^{-\phi}$, with scaling ex-

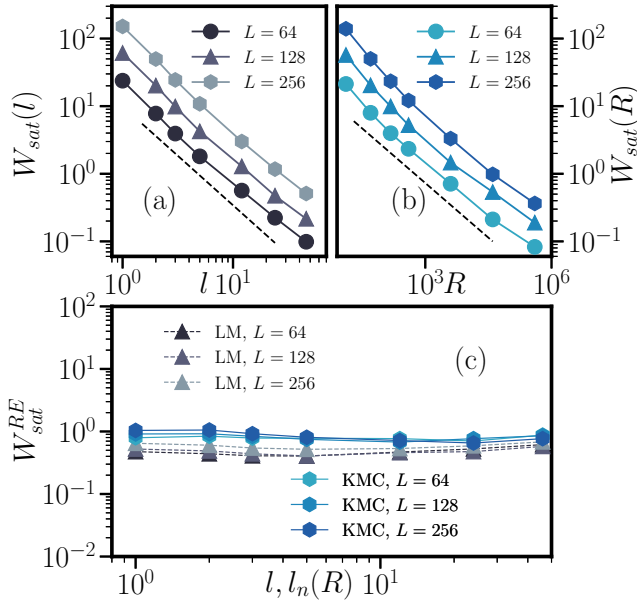


FIG. 13. (a) Scaling of the saturation roughness $W_{sat}(l)$ in the LM model as function of the average diffusion length l with optimal values for σ^2 for different system sizes L . The black dotted line follows $\sim l^{-3/2}$. (b) Scaling of $W_{sat}(R)$ as function of the growth parameter R . The black dotted line follows $\sim R^{-1/2}$. (c) Rescaled saturation roughness W_{sat}^{RE} in the LM model and corresponding KMC simulations.

ponent $\phi \approx 3/2$ that is independent of L . For KMC simulations we find that the saturation roughness decreases with increasing value of the growth parameter R according to $W_{sat}(L, R) \sim R^{-\delta}$, with $\delta \approx 1/2$ [see Fig. 13 (b)]. To unveil the connection of the scaling exponents ϕ and δ , we recall that $l = l_n(R) \sim R^\gamma$, with $\gamma = 1/3$ [see Eq. 13 and Fig. (3)]. Thus, the exponents of both models are connected by γ via $\phi = \delta/\gamma = 3/2$. To further confirm the correctness of the scaling exponents ϕ and δ , we define a rescaled saturation roughness for both models, $W_{sat}^{RE} = W_{sat}(L, l)/(L^\alpha l^{-\phi})$ (LM) and $W_{sat}^{RE} = W_{sat}(L, R)/(L^\alpha R^{-\delta})$ (KMC). Results for W_{sat}^{RE} in both cases are shown in Fig. 13 (c). We find that W_{sat}^{RE} as function of l (LM model) is indeed a constant. The same holds for KMC simulations where W_{sat}^{RE} is plotted as function of $l_n(R)$.

3. Fluctuations of the saturated interface width

To further show the equality of the resulting morphologies generated by both models in the regime of saturated interface width, we compare the fluctuations of W_{sat} in the KMC and the LM model for $L = 128$. To this end, we calculate the squared roughness in the asymptotic regime ($\theta \geq \theta^*$) of the interface width

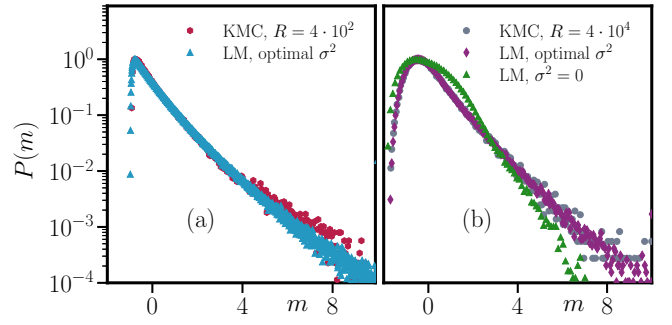


FIG. 14. Distribution of the squared roughness $P(m)$ in the steady-state, where W_{sat} has been reached. Here, $m = (w_2 - \langle w_2 \rangle)/\sigma_{w_2}$. The value of R in the KMC model in (a) is $R = 10^2$ and $l = 5$ (optimal $\sigma^2 = 0.1$) in the LM model. In (b), $R = 10^4$ and $l = 24$ (optimal $\sigma^2 = 7.0$). The system size is $L = 128$ in (a) and (b).

$$w_2 = \frac{1}{L} \sum_{i=1}^L (h_i(\theta) - \langle h(\theta) \rangle)^2, \quad (23)$$

and measure the distribution of w_2 , which is expected to follow

$$P(w_2) = \frac{1}{\sigma_{w_2}} \Phi \left(\frac{w_2 - \langle w_2 \rangle}{\sigma_{w_2}} \right). \quad (24)$$

Here, $\Phi(m)$ is a scaling function with $m = (w_2 - \langle w_2 \rangle)/\sigma_{w_2}$, and

$$\sigma_{w_2} = \sqrt{\langle w_2^2 \rangle - \langle w_2 \rangle^2} \quad (25)$$

represents the root mean square deviation of w_2 . Results at two representative values of R and corresponding $P(l | l_n, \sigma^2)$ are shown in Fig. 14. We observe that $P(m)$ at $R = 4 \cdot 10^2$ is more sharply peaked around $m = 0$ compared to $R = 4 \cdot 10^4$. We find good agreement of $P(m)$ in both models for both considered growth conditions which means that the interface fluctuations in the asymptotic regime behave identical in both models. In Fig. 14 (b) we additionally plot $P(m)$ for the LM model with $\sigma^2 = 0$ (green data set). The data reflect again the importance of adding fluctuations ($\sigma^2 > 0$) to the diffusion length l in the LM model.

IV. CONCLUSIONS AND OUTLOOK

In this work, we have introduced an extended limited mobility (LM) model for nonequilibrium surface growth, which is capable of predicting *low* temperature MBE growth for arbitrary values of the growth parameter R . Compared to earlier versions of the LM model, particularly the DT model, our extension concerns the diffusion length l which we treat as a variable parameter.

To relate our LM model to another standard model for surface growth, namely KMC, we proposed to set l equal to the nucleation length resulting from short KMC simulations for the particle displacements. We tested this ansatz by comparing LM and KMC results for the cluster evolution during submonolayer growth. While the LM model with fixed l works well at small values of the growth parameter R , this is not the case at larger R . As a next step, we therefore included fluctuations to the diffusion length of particles in the LM model. Specifically, we employed a Gaussian distribution where the mean is given by the nucleation length extracted from KMC, whereas the variance is fitted to match the number of clusters in KMC simulations during growth in the submonolayer regime.

Turning towards multilayer growth, we compared layer coverages for different growth conditions and found excellent agreement between both models. Moreover, we analyzed in detail the global interface width for different system sizes up to coverages deep in the regime of saturated surface roughness. Not only is transient regime of the global interface width identical in both models, but also the crossover coverage where saturation is reached. Additionally, we find that by using our LM model with variable diffusion length, also the values of the saturation roughness match in both models for all considered system sizes and values of the growth parameter of the KMC simulations. A scaling analysis revealed that the LM model belongs to the VLDS universality class for arbitrary diffusion lengths. Considering the distribution of the saturated surface roughness shows again that agreement between both models can only be achieved if fluctuations to the diffusion length in the LM model are included. Thus, we conclude that the surface evolution in the KMC model for arbitrary values of the growth parameter R is correctly reproduced by the LM model at any stage of surface growth.

The present model can be extended in various directions. First, it is possible to modify the model such that it also mimics MBE growth at *high* temperatures where detachment of particles is present. This may be achieved by using the transition rules of the Wolf-Villain model [27, 28] (with variable diffusion length) rather than those of the DT model. Second, the effect of an additional energy barrier for interlayer diffusion processes across step-edges, usually referred to as Ehrlich-Schwoebel barrier, can be included to account for growth instabilities that are responsible for the formation of quasiregular mounds. Normally, in presence of such a barrier, KMC simulations are slowed down due to the sampling of diffusion trajectories of free particles on top of clusters. A physically reasonable treatment of an Ehrlich-Schwoebel barrier in our LM model would lead to a further computational speedup compared to KMC simulations.

Finally, we give a brief outlook towards a further important extension of our model, that is, surface growth in two dimensions. We have performed various test calculations indicating that our extended LM model (with

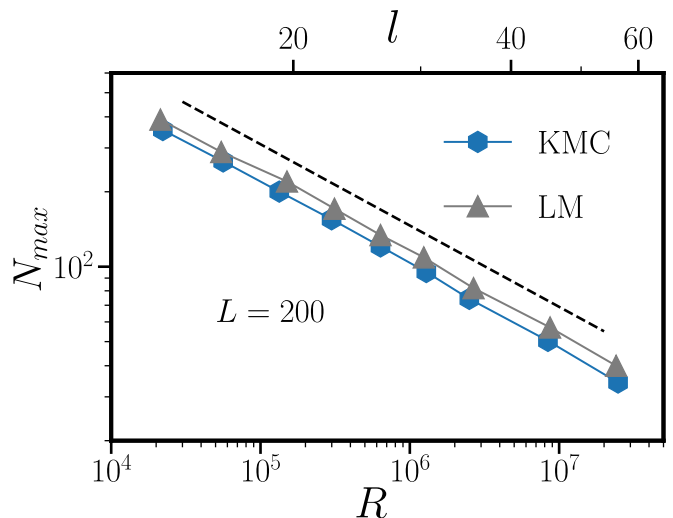


FIG. 15. N_{max} in the submonolayer growth regime on two-dimensional substrates of lateral size $L = 200$ for various growth conditions in the KMC and the LM model, respectively. The black dotted line follows $\sim R^{-1/3}$.

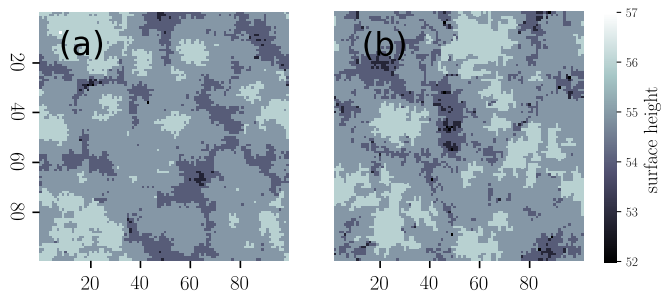


FIG. 16. (a) Exemplary lattice structure (of size 100×100) from KMC simulations with $R = 2 \cdot 10^4$ at $\theta = 50$. (b) Lattice structure obtained from the LM model with $l = 13.1$ and $\sigma^2 = 7.2$ at the same coverage, $\theta = 50$.

fluctuating diffusion length and an optimized variance) can indeed reproduce KMC results also in two dimensions. As a glimpse in this direction, we show in Fig. 15 results for N_{max} as function of R (KMC) and l (LM), respectively (submonolayer regime). It is seen that the two models yield consistent results. Representative lattice structures in the multilayer regime for the coverage $\theta = 50$ are shown in Fig. 16. One observes good agreement regarding the surface heights, even though the island shape is somewhat different. This mismatch may be cured by properly modifying the choice for the final lattice site of deposited particles. Nonetheless, we consider these results as encouraging to perform further simulations in the physically relevant two-dimensional case.

ACKNOWLEDGMENTS

This work was funded by the Deutsche Forschungsgemeinschaft (DFG, German Research Foundation) - Projektnummer A7 - SFB 951.

-
- [1] M. Y. Yao, F. Zhu, C. Q. Han, D. D. Guan, C. Liu, D. Qian, and J. F. Jia, *Sci. Rep.* **6**, 213226 (2016).
- [2] J. M. Wofford, S. Nakhaie, T. Krause, X. Liu, M. Ramsteiner, M. Hanke, H. Riechert, and J. M. J. Lopes, *Sci. Rep.* **7**, 43644 (2017).
- [3] L. Jin, D. Zhang, H. Zhang, J. Fang, Y. Liao, T. Zhou, C. Liu, Z. Zhong, and V. G. Harris, *Sci. Rep.* **6**, 34030 (2016).
- [4] P. S. Tobin, S. M. Vernon, C. Bajgar, S. Wojtczuk, M. R. Melloch, A. Keshavarzi, T. B. Stellwag, S. Venkatensan, M. Lundstrom, and K. A. Emery, *IEEE Trans. Electron Dev.* **37**, 469-477 (1990).
- [5] A. L. Barabasi and H. E. Stanley, *Fractal Concepts in Surface Growth*, Cambridge University Press (1995).
- [6] A. Pimpinelli and J. Villain, *Physics of Crystal Growth*, Cambridge University Press (1998).
- [7] T. Michely and J. Krug, *Islands, Mounds and Atoms*, Springer (2003).
- [8] J. W. Evans, P. A. Thiel, and M. C. Bartelt, *Surf. Sci. Rep.* **61**, 1 (2006).
- [9] S. Bommel, N. Kleppmann, C. Weber, P. Schäfer, J. Novak, S. V. Roth, F. Schreiber, S. H. L. Klapp, and S. Kowarik, *Nat. Comm.* **5**, 5388 (2014).
- [10] M. Hohage, M. Bott, M. Morgenstern, Z. Zhang, T. Michely, and G. Cosma, *Phys. Rev. Lett.* **76**, 2366 (1996).
- [11] J. D. Weeks and G. H. Gilmer, *Advances in Chemical Physics* **40** (1979).
- [12] P. A. Maksym, *Semicond. Sci. Technol.* **3**, 594 (1988).
- [13] M. Kotrla, *Computer Physics Communications* **97**, 82-100 (1996).
- [14] A. C. Levi and M. Kotrla, *J. Phys.: Condens. Matter* **9**, 299 (1997).
- [15] T. Martynec and S. H. L. Klapp, *Phys. Rev. E* **98**, 042801 (2018).
- [16] N. Kleppmann, and S. H. L. Klapp, *Phys. Rev. B* **91**, 045436 (2015).
- [17] N. Kleppmann, and S. H. L. Klapp, *J. Chem. Phys.* **142**, 064701 (2015).
- [18] N. Kleppmann, and S. H. L. Klapp, *Phys. Rev. B* **94**, 241404(R) (2016).
- [19] M. Oettel, M. Klopotek, M. Dixit, E. Empting, T. Schilling, and H. Hansen-Goos, *J. Chem. Phys.* **145**, 074902 (2016).
- [20] M. Klopotek, H. Hansen-Goos, M. Dixit, T. Schilling, F. Schreiber, and M. Oettel, *J. Chem. Phys.* **146**, 084903 (2017).
- [21] P. K. Jana, and A. Heuer, *J. Chem. Phys.* **138**, 124708 (2013).
- [22] S. Clarke and D. D. Vvedensky, *J. Appl. Phys.* **63**, 2272 (1988).
- [23] P. Kratzler and M. Scheffler, *Phys. Rev. Lett.* **88**, 036102 (2002).
- [24] D. J. Godbey, J. V. Lill, and J. Deppe, *Appl. Phys. Lett.* **65**, 711 (1994).
- [25] Y. Nie, C. Liang, P. R. Cha, L. Colombo, R. M. Wallace and K. Cho, *Sci. Rep.* **7**, 2977 (2017).
- [26] F. Family, *Physica A*, **168**, 561-580 (1990).
- [27] D. E. Wolf and J. Villain, *Europhys. Lett.* **13**, 389 (1990).
- [28] J. Villain, *J. Phys. I* **1**, 19 (1991).
- [29] S. Das Sarma and P. Tamborenea, *Phys. Rev. Lett.* **66**, 325 (1991).
- [30] S. Das Sarma and S. V. Ghaisas, *Phys. Rev. Lett.* **69**, 3762 (1992).
- [31] Z. W. Lai and S. Das Sarma, *Phys. Rev. Lett.* **66**, 2348 (1991).
- [32] C. Herring, *J. Appl. Phys.* **21**, 301 (1950).
- [33] W. W. Mullins, *J. Appl. Phys.* **28**, 333 (1957).
- [34] S. Das Sarma, P. Punyindu Chatrathorn, and Z. Toroczkai, *Phys. Rev. E* **65**, 036144 (2002).
- [35] B. Mal, S. Ray, and J. Shamanna, *Eur. Phys. J. B* **82**, 341-347 (2011).
- [36] B. Mal, S. Ray, and J. Shamanna, *AIP Conference Proceedings* **1832**, 040021 (2017).
- [37] F. D. A. Aaro Reis, *Phys. Rev. E*, **81**, 041605 (2010).
- [38] T. B. T. To, V. B. Sousa, F. D. A. Aaro Reis, *Physica A* **511**, 240-250 (2018).
- [39] J. M. Kim and J. M. Kosterlitz, *Phys. Rev. Lett.* **62**, 2289 (1989).
- [40] D. E. Wolf and J. Kertesz, *Phys. Rev. Lett.* **63**, 1191 (1989).
- [41] P. Punyindu Chatrathorn and S. Das Sarma, *Phys. Rev. E* **57**, 4863(R) (1998).
- [42] P. Punyindu Chatrathorn and S. Das Sarma, *Phys. Rev. E* **66**, 041601 (2002).
- [43] P. Punyindu Chatrathorn Z. Toroczkai, and S. Das Sarma, *Phys. Rev. B* **64**, 205407 (2001).
- [44] F. Family and T. Vicsek, *J. Phys. A* **18**, L75-L81 (1985).
- [45] P. M. Richards, *Phys. Rev. B* **43**, 6750 (1991).
- [46] A. Chame and F. D. A. Aaro Reis, *Surf. Sci.* **553**, 145-154 (2004).
- [47] M. Kardar, G. Parisi, and Y. C. Zhang, *Phys. Rev. Lett.* **56**, 889 (1986).
- [48] K. A. Takeuchi, M. Sano, T. Sasamoto, and H. Spohn (2011), *Sci. Rep.* **1**, 34 (2011).
- [49] L. Bertini and G. Giacomin, *Comm. in Math. Phys.*, **183**, 571-607 (1997).
- [50] J. Krug and H. Spohn, *Phys. Rev. A* **38**, 4271 (1988).
- [51] J. Krug, M. Plischke, and M. Siegert, *Phys. Rev. Lett.* **70**, 3271 (1993).
- [52] G. Ehrlich and F. G. Hudda, *J. Chem. Phys.* **44**, 1039 (1966).
- [53] R. L. Schwoebel and E. J. Shipsey, *Journal of Applied Physics* **37**, 3682 (1966).
- [54] R. L. Schwoebel, *Journal of Applied Physics* **40**, 614 (1969).
- [55] J. G. Amar and F. Family, *Phys. Rev. Lett.* **74**, 11 (1995).

- [56] F. D. A. Aaro Reis, Phys. Rev. E **70**, 031607 (2004).
- [57] J. H. Neave, B. A. Joyce, P. J. Dobson, and N. Norton, Appl. Phys. A **31**, 1-8 (1983).
- [58] F. Alexandre, L. Goldstein, G. Leroux, M. C. Joncour, H. Thibierge, and E. V. K. Rao, Journal of Vacuum Science and Technology B **3**, 950 (1985).
- [59] R. Kunkel, B. Poelsema, L. K. Verheij, and G. Comsa, Phys. Rev. Lett. **65**, 733 (1990).
- [60] P. Šmilauer, M. R. Wilby, and D. D. Vvedensky, Phys. Rev. B **47**, 4119 (1993).
- [61] T. A. de Assis and F. D. A. Aaro Reis, J. Stat. Mech. P10008 (2013).
- [62] T. A. de Assis and F. D. A. Aaro Reis, J. Stat. Mech. P06023 (2015).
- [63] R. Burioni, Phys. Rev. E **51**, 5426 (1995).
- [64] S. C. Park, J. M. Park, and D. Kim, Phys. Rev. E **65**, 015102(R) (2001).